

Article

The Impacts of Vegetation and Meteorological Factors on Aerodynamic Roughness Length at Different Time Scales

Mingzhao Yu ^{1,2}, Bingfang Wu ^{1,2,*}, Hongwei Zeng ¹, Qiang Xing ¹ and Weiwei Zhu ¹

¹ Key Laboratory of Digital Earth Science, Institute of Remote Sensing and Digital Earth, Chinese Academy of Sciences, Olympic Village Science Park, W. Beichen Road, Beijing 100101, China; yumz@radi.ac.cn (M.Y.); zenghw@radi.ac.cn (H.Z.); xingqiang@radi.ac.cn (Q.X.); zhuww@radi.ac.cn (W.Z.)

² College of Resources and Environment, University of Chinese Academy of Sciences, Beijing 100049, China

* Correspondence: wubf@radi.ac.cn; Tel.: +86-10-6485-5689

Received: 27 February 2018; Accepted: 10 April 2018; Published: 16 April 2018



Abstract: The aerodynamic roughness length (z_{0m}) is a crucial parameter for reliably simulating turbulent exchanges between the land surface and the atmosphere. Due to the large number of input variables related to vegetation growth and aerodynamic conditions near the surface, estimating z_{0m} precisely is difficult and, to date, no universal model has been established. Understanding the z_{0m} changes in time series data and the relative contributions of vegetation indices and meteorological factors is important to providing a basis for modelling z_{0m} . In this paper, the main meteorological factors that influence z_{0m} in different seasons are presented based on data from three automatic weather stations (AWSs) that represent various land surface patterns in the Heihe river basin. A correlation analysis identified the dominant factors that influence z_{0m} changes at half-hour and daily scales; then, a factor analysis was performed to identify the different contributions of vegetation indices and meteorological factors to z_{0m} at different time scales. The results show that meteorological factors (wind speed, wind direction and atmospheric stability) are the main driving factors for z_{0m} at the Arou and Guantan sites, which are situated in grassland and forest mountain areas, respectively, and that the vegetation indices have no impact on the z_{0m} variations in these areas. In contrast, for the Daman site, situated in flat farmland, the vegetation indices are the primary driving factors, while meteorological factors such as wind speed and atmospheric stability are secondary factors, and wind direction has no significant influence. Finally, a detailed analysis was conducted to detect the relationships between half-hourly z_{0m} measurements and three dominant meteorological factors.

Keywords: aerodynamic roughness length; Heihe river basin; factor analysis

1. Introduction

The aerodynamic roughness length (z_{0m}) is the height above the ground where the wind speed is zero under neutral conditions [1]. Aerodynamic roughness length is a key variable in land surface flux simulations and atmospheric boundary studies [2,3]. The z_{0m} metric is a virtual height under ideal atmospheric conditions that cannot be measured and quantified directly; therefore, it is important to develop a reliable parameterized method for estimating z_{0m} at different spatial and temporal scales.

Micrometeorological wind profiles measurements have generally been used to estimate site-specific z_{0m} based on the Monin–Obukhov similarity theory [4,5]. However, because modern studies involve land surface processes at a greater spatial scale, in recent years, an increasing number of models have been established to estimate regional z_{0m} . Raupach developed an approach for estimating z_{0m} in terms of height, width, spacing and wind-drag properties of surface roughness elements [6,7], Jasinsk simulated the parameters in the Raupach model by classifying four vegetation

types [8]. With the development of remote sensing techniques, links have been built between regional z_{0m} and vegetation indices such as the normalized different vegetation index (NDVI) and leaf area index (LAI) [9,10]. In addition, the signatures of bidirectional reflectance distribution function (BRDF) derived from multi-angle remote sensing data have been used to describe the canopy structural components of roughness length [11]. However, previous studies of modelling z_{0m} mainly considered topographic and vegetation features on the surface and neglected the effects of aerodynamic factors, which results in significant errors [12]. Schmid found that z_{0m} is not only related to the vegetation geometry but is also affected by the near-surface wind speed [13]. Zhou found that z_{0m} changes with wind direction and atmospheric stability at a given location [14,15]. However, few quantitative studies have been performed to evaluate the proportions of all the factors that may influence the instantaneous or daily average z_{0m} estimates over different underlying surfaces.

Therefore, to fill this gap in the field and provide a reference for modelling regional z_{0m} , this paper investigates the driving factors of z_{0m} using onsite time-series data over three typical vegetation types. Depending on research and application needs, z_{0m} can be summarized to hourly or daily data or even fixed within a specified season; we select half-hourly z_{0m} and daily z_{0m} as the main objectives in this study. Several statistical methods are available to quantify the effects of various factors on z_{0m} , including regression analysis, principal component analysis (PCA), factor analysis and artificial neural network analysis. Considering that all observed variables mainly reflect changes of z_{0m} in a certain place in two ways—growth of vegetation and variations of atmospheric conditions—we adopt factor analysis in this study to search for joint factors and evaluate the contributions of factors related to z_{0m} .

In recent decades, intensive ground observation facilities supported by continuous research projects have been established in the Heihe River basin, and these facilities have collected multiple meteorological data time-series [16–18] which are convenient for analysing the differences between the factors that influence z_{0m} over different landform and vegetation types in a single climate zone. For this study, we selected the Guantan, Arou and Daman stations, which respectively represent underlying surfaces of forest, grassland and cropland. Vegetation indices calculated from remotely sensed images are used to describe the vegetation growth. Finally, a detailed analysis of the variation characteristics of half-hourly z_{0m} is presented, along with each main driving meteorological factor.

2. Data and Study Area

2.1. Site Description

In this study, data were collected from field automatic weather stations (AWSs) at three sites in the Heihe River basin distributed in the upper and middle reaches (Figure 1). Arou station is located in an east–west oriented valley with a maximum width of 3 km from north to south. The site is surrounded by natural alpine meadow with grass reaching a height of approximately 20–30 cm during the growing season. The Guantan site is surrounded by continuous mountains with elevations ranging from 2700–3400 m, and the weather station is located on the shady slope of the mountain in the Dayekou sub-catchment. The overstory tree species at the study site is Qinghai spruce, and the forest floor is nearly covered by a layer of moss with a depth of 10 cm [19]. Daman station is located in a typical oasis on very flat terrain near Zhangye City. The underlying surface is mainly irrigated maize that reaches a maximum height of approximately 180 cm [20].

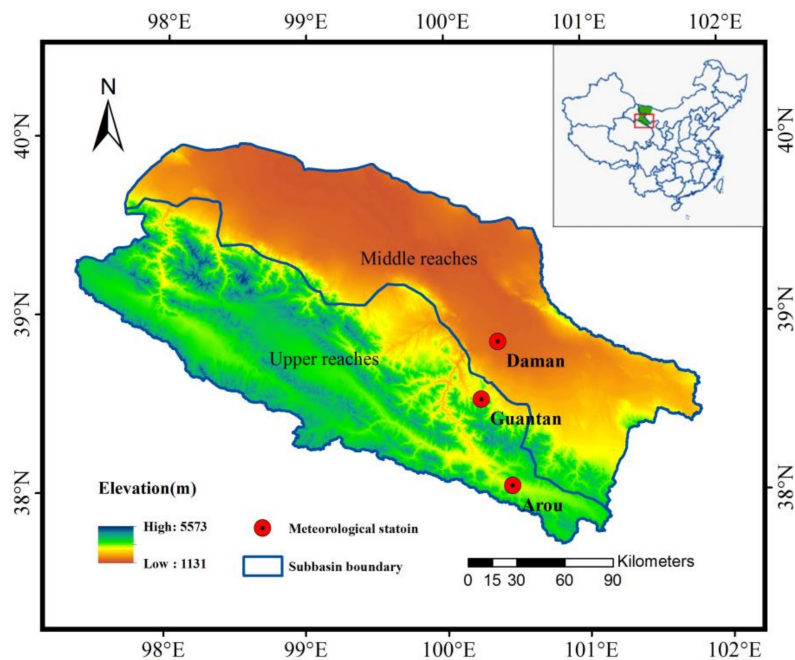


Figure 1. Locations of the three automatic weather stations (AWSs) in the Heihe River basin. The elevation map was produced using the ASTER GDEM product of METI and NASA (available online: <http://www.gdem.aster.ersdac.or.jp>).

2.2. Data

2.2.1. Onsite Data

The AWSs at these three sites collected 144 records per day including wind speed, wind direction, air temperature and air humidity at 10-min intervals at different heights. A description of the AWSs and the time periods covered by the data used in this study are listed in Table 1.

Table 1. Description of the three used AWSs.

Location	Coordinates	Altitude (m)	Land Use	Sensor Height (m)	Period	Data Logger
Arou	38°2'50'' N, 100°27'51'' E	3033	Alpine meadow	1, 2, 5, 10, 15, 25	1 May 2014– 31 October 2014	CR23X
Guantan	38°32'1'' N, 100°15'0'' E	2835	Qinghai spruce	2, 10, 24	1 May 2011– 31 October 2011	CR23XTD
Daman	38°51'20'' N, 100°22'20'' E	1556	Spring maize	3, 5, 10, 15, 20, 30, 40	1 May 2014– 31 October 2014	CR800

2.2.2. Satellite Data

Remotely sensed vegetation indices including the normalized difference vegetation index (NDVI) and leaf area index (LAI) were selected as the key indicators to measure the characteristic of vegetation growth. The time-series cloud-masked NDVI values of the sites were calculated using the MODIS red and infrared band reflectance after atmospheric correction: 2010 for the Guantan station and 2012 for the Arou station with 1 km resolution. The Savitzky–Golay (SG) filter was adopted to fill gaps to acquire the daily NDVI [21]. The 1-km/5-day composite LAI product in the Heihe River basin was acquired from the China science data centre (available online: <http://card.westgis.ac.cn/>), which consists of a normalization algorithm to integrate Terra-MODIS, Aqua-MODIS, FY3A-MERSI and FY3B-MERSI data. The time-continuous LAI were retrieved using neural networks and a maximum-value compositing algorithm [22–24].

3. Methods

3.1. Calculation of the Obukhov Length L

The Obukhov length L near the surface can be used to characterize the effect of atmospheric stability on the turbulence [25]. Therefore, this study investigates the implications of vertical measurement profiles in relation to the Monin–Obukhov similarity, using the gradient Richardson number (Ri) to infer L with the following equations :

$$L = \begin{cases} z / Ri & \text{when } Ri < 0 \\ z(1 - 5Ri) / Ri & \text{when } Ri > 0 \end{cases} \quad (1)$$

where $z = (z_1 - z_2) / \ln(z_1 / z_2)$ is the height where the calculated Richardson number is valid, z_1 is fixed at 10 m height, while z_2 is 2 m for Arou and Guantan site and 3 m for Daman site, respectively. Compared to L, Ri has the advantage that it contains only meteorological gradients that can be determined experimentally. Ri is expressed as the non-dimensional ratio between the buoyancy forces and the inertial ones due to the wind [26]. The sign of this number is determined by the temperature gradient, the negative values are an index of instability and the positive ones are an index of stability.

$$Ri = \frac{g(\partial\theta_v/\partial z)}{\bar{T}(\partial u/\partial z)^2} \quad (2)$$

where \bar{T} is a reference atmospheric temperature, $\partial\theta_v/\partial z$ is the difference in virtual potential temperature (VPT) between two measurements at heights z_1 and z_2 , $g = 9.8 \text{ m/s}^2$ is the gravitational acceleration, and $\partial u/\partial z$ is the wind gradient between z_1 and z_2 .

3.2. Calculating the Aerodynamic Roughness Length from AWS Data

To guarantee the reliability of the wind profile results, the raw datasets were pre-processed and quality control was performed to obtain aerodynamic roughness values based on the following criteria: (1) the minimum wind velocity of all layers exceeded 2 m/s; (2) data obtained at rainy times were discarded; (3) missing or invalid data were interpolated based on neighbouring data [18,27].

The aerodynamic surface roughness length can be determined iteratively based on wind profile data. Using the Monin–Obukhov similarity, the z_{0m} values can be calculated via the logarithmic wind profile equation [6,7]:

$$u = \frac{u_*}{k} \left[\ln\left(\frac{z-d}{z_{0m}}\right) - \Psi_m\left(\frac{z-d}{L}\right) \right] \quad (3)$$

$$\theta = \frac{\theta_*}{k} \left[\ln\left(\frac{z-d}{z_{0h}}\right) - \Psi_h\left(\frac{z-d}{L}\right) \right] + \theta_0 \quad (4)$$

where u and θ denote the wind speed and potential air temperature, respectively, at the height z above ground level, u_* is the friction velocity, θ_* is the friction temperature; k is von Karman’s constant ($k = 0.4$); d is the zero-plane displacement; z_{0m} is the aerodynamic roughness length; z_{0h} is the thermal roughness length and θ_0 is the potential temperature near the surface. The expressions of the stability functions Ψ_m and Ψ_h depend on the stability conditions in the surface layer, which are described by the stability parameter Z/L [28].

When $Z/L < 0$ (unstable conditions) [29],

$$\Psi_m = \ln \frac{1+x^2}{2} + 2 \ln \frac{1+x}{2} - 2 \arctg x + \frac{\pi}{2} \quad (5)$$

$$\Psi_h = 2 \ln \frac{1+y}{2} \quad (6)$$

$$x = \left(1 - 15 \frac{z-d}{L}\right)^{\frac{1}{4}}, y = \left(1 - 16 \frac{z-d}{L}\right)^{\frac{1}{2}} \quad (7)$$

When $Z/L > 0$ (stable conditions) [30],

$$\Psi_m = \Psi_h = -5 \frac{z-d}{L} \quad (8)$$

In this study, we use the least-squares method to determine z_{0m} [31,32]. Equation (3) can be written as the following simplified form:

$$u = ax + b \quad (9)$$

where $a = u_*/k$, $x = \ln(z-d) - \Psi_m$ and $b = -\ln z_{0m} \cdot a$. Commonly, d is related to the vegetation height (h) such that d equals $0.67h$ over surfaces covered by dense and homogeneous vegetation [33]. Therefore, d is determined here by iterating over 0.1 m intervals of from 0.1 m to 3 m. For each given d , a correlation coefficient exists for the fitting Equation (9), and the optimal d value is chosen when the correlation coefficient reaches its maximum, the invalid value will be returned in loop iterations if the wind speed gradient is abnormal. Finally, the 10-min z_{0m} values can be calculated according to the optimal d value. To maximally avoid effects from missing data, the z_{0m} data are averaged over 30-min intervals and daily average z_{0m} values are also calculated.

3.3. Correlation Analysis

Correlation coefficients measure the strength and direction of a relationship between two variables. Here, Pearson product-moment correlation coefficients were calculated to investigate the relationship between the latent factors and z_{0m} . We selected the NDVI and the LAI as the most likely factors that represent the effects of vegetation growth on z_{0m} and adopted wind speed (WS), wind direction (θ), relative humidity (RH), air temperature (T), Obukhov length (L) and air pressure (P) as the meteorological factors. Because Obukhov length is an instantaneous parameter that describes atmospheric conditions, calculating an average daily level of Obukhov length is meaningless and excluded from the correlation analysis of daily z_{0m} . To match the half-hourly z_{0m} data, we used daily NDVI and LAI values under the assumption that changes in vegetation indices can be ignored over shorter periods. Because wind direction is a categorical variable, we proposed a definition of wind deflection angle ($\Delta\theta$) between the prevailing wind direction (θ_p) and the instantaneous wind direction, described as follows:

$$\Delta\theta = \begin{cases} |\theta - \theta_p| & \text{when } |\theta - \theta_p| < 180 \\ 360 - |\theta - \theta_p| & \text{when } |\theta - \theta_p| > 180 \end{cases} \quad (10)$$

The prevailing wind direction usually depends on the local topography, latitude and the locations of land and sea; therefore, $\Delta\theta$ is categorized as a topographic factor in the subsequent factor analysis. The prevailing wind directions at the Arou, Guantan and Daman sites are 162° , 121° and 318° relative to due north, respectively, according to all observation data.

3.4. Factor Analysis

Factor analysis is a statistical method for decomposing input data as a linear combination of common factors and specific factors in a lower dimensional space. As a feature extraction approach, it seeks to acquire factor scores for input data in a lower dimensional space via a linear transformation. Those factor scores can be viewed as extracted features of the original data in another, lower-dimensional space. In this study, we first used correlation analysis to determine the main driving factors that influence the changes in z_{0m} at half-hourly and daily intervals. Then, the main driving factors were normalized to eliminate the differences in dimensions between the variables:

$$X'_j = \frac{X_j - \bar{X}_j}{\sigma_j} \quad (11)$$

where X_j is the indicator value of the j factor, and \bar{X}_j and σ_j are the average and standard deviation of all the sample data of the j factor, respectively. Then, factor analysis was performed to determine the contributions of the vegetation indices and meteorological factors that affect z_{0m} . The mathematical model of factor analysis is as follows [34]:

$$X'_{k \times 1} = A_{k \times n} F_{n \times 1} + \epsilon_{k \times 1} \tag{12}$$

where $X' = (X'_1, X'_2, \dots, X'_j, \dots, X'_k)$ is a k -dimensional stochastic vector composed of k samples, $F = (F_1, F_2, \dots, F_n)$ is the common factor of X' ($n < k$), $\epsilon_{k \times 1}$ is an unobserved stochastic error factor with zero mean and finite variance and $A_{k \times n}$ is the correlation coefficient matrix of the top n factors:

$$A_{k \times n} = \begin{bmatrix} a_{11} & \cdots & a_{1n} \\ \vdots & \ddots & \vdots \\ a_{k1} & \cdots & a_{kn} \end{bmatrix} = \begin{bmatrix} u_{11}\sqrt{\lambda_1} & \cdots & u_{1n}\sqrt{\lambda_n} \\ \vdots & \ddots & \vdots \\ u_{k1}\sqrt{\lambda_1} & \cdots & u_{kn}\sqrt{\lambda_n} \end{bmatrix} \tag{13}$$

where $\lambda_1, \lambda_2, \dots, \lambda_n$ are the first n characteristic values of the covariance matrix $X'_{k \times 1}$, and u_1, u_2, \dots, u_n are the corresponding standard orthogonal eigenvectors. Based on the number of eigenvalues that exceed 1, the amounts of the common factors, n , can be determined. Then, the variance contribution of the common factor $F_{n \times 1}$ is obtained by calculating the sum of the squares of the elements in the j -th column of $A_{k \times n}$:

$$S_j = \sum_{i=1}^n a_{ij}^2, \quad j = 1, 2, \dots, n \tag{14}$$

which represents the sum of the variance contributions of the same common factor F_j to the variable. The cumulative contributions of the common factors can then be calculated accordingly. The factor analysis was performed using SPSS version 25 software (IBM, New York, NY, USA), using PCA as the extraction method and varimax as the rotation method.

4. Results

4.1. Driving Factors for Changes in Half-Hourly and Daily z_{0m}

The results of bivariate correlation analyses between half-hourly z_{0m} , daily z_{0m} and each possible driving factor are shown in Table 2, which indicates that the main driving factors for z_{0m} differ among the three stations. For the Arou and Guantan sites, the half-hourly and daily z_{0m} values are positively correlated with the wind deflection angle and negatively correlated with the wind speed, while no significant correlation exists with the NDVI and the LAI, which represent the vegetative growth conditions. In contrast, at the Daman site, the half-hourly and daily z_{0m} values are positively correlated with the NDVI and the LAI and negatively correlated with wind speed, while the wind deflection angle has no correlation to z_{0m} . Similarly, half-hourly z_{0m} is significantly correlated with the Obukhov length; however, neither half-hourly z_{0m} nor daily z_{0m} have any significant correlation with relative humidity, air temperature or air pressure at any of the sites. The factors that are significantly correlated with half-hourly z_{0m} and those that are significantly correlated with daily z_{0m} were selected to conduct a subsequent factor analysis. As Table 2 shows, only two factors have significant correlations with daily z_{0m} at the Arou and Guantan sites; therefore, it is unnecessary to conduct a factor analysis. Consequently, we conducted the factor analysis for daily z_{0m} only at the Daman site and for half-hourly z_{0m} at all three sites.

Table 2. The correlation coefficients (*R*) between half-hourly z_{0m} , daily z_{0m} and possible driving factors.

Factors	Arou z_{0m}		Guantan z_{0m}		Daman z_{0m}	
	Half-Hourly	Daily	Half-Hourly	Daily	Half-Hourly	Daily
WS	−0.592 **	−0.488 **	−0.409 **	−0.326 *	−0.326 *	−0.345 *
$\Delta\theta$	0.574 **	0.641 **	0.725 **	0.407 **	0.027	0.123
RH	0.274	0.040	0.137	0.093	0.011	0.061
T	−0.125	−0.200	0.223	0.180	0.149	0.263
L	0.608 **	-	0.602 **	-	0.542 **	-
P	0.113	0.079	0.276	0.151	0.009	0.056
NDVI	0.161	0.282	0.018	0.130	0.546 **	0.639 **
LAI	0.081	0.177	−0.069	0.052	0.571 **	0.671 **

An asterisk (*) denotes a correlation significant at the 0.05 level; A double asterisk (**) denotes a correlation significant at the 0.01 level.

4.2. Contributions of Driving Factors to Half-Hourly z_{0m}

Before conducting the factor analysis, Kaiser–Meyer–Olkin (KMO) [35] and Bartlett’s sphericity tests [36] were applied to examine the appropriateness of the data for factor analysis. The KMO test determines the degree of correlation between variables with partial correlation coefficients: the KMO values for the half-hourly z_{0m} values at the Arou, Guantan and Daman sites were 0.625, 0.591 and 0.703, respectively, all of which satisfy the minimal requirement; that is, they are above 0.5. Bartlett’s sphericity test determines whether variables are independent based on the variables’ correlation coefficient matrixes. The Bartlett’s sphericity test results were 67.222, 58.761 and 121.928 at the Arou, Guantan and Daman sites, respectively, and the *p*-value for each site was 0: all of these satisfy the requirement that *p* should be below 0.001. Based on the results of these two tests, the data are suitable for factor analysis.

Tables 3 and 4 show the factor analysis results. For half-hourly z_{0m} at the Arou and Guantan sites, the first common factors are wind speed and Obukhov length, which are aerodynamic factors (A_factor): their contributions for Arou and Guantan are 44.03% and 42.87%, respectively. The second common factor (the topographic factor (T_factor)) is mainly expressed by wind deflection angle, and the contributions at Arou and Guantan are 38.33% and 38.66%, respectively. For the Daman site, the first common factor is the vegetation factor (V_factor) consisting of NDVI and LAI: the factor loads for NDVI and LAI are 0.959 and 0.941, respectively. The contribution of the vegetation factor is 53.14%. The aerodynamic factor, composed of wind speed and Obukhov length, is a secondary factor that contributes of 30.29%.

Table 3. Rotated component matrix in factor analysis.

Factors	Arou Half-Hourly		Guantan Half-Hourly		Daman Half-Hourly		Daman Daily	
	A_Factor	T_Factor	A_Factor	T_Factor	V_Factor	A_Factor	V_Factor	A_Factor
WS	−0.765	−0.003	−0.799	−0.232	−0.239	−0.514	−0.350	−0.667
$\Delta\theta$	−0.042	0.998	−0.026	0.829	-	-	-	-
L	0.764	−0.052	0.662	0.095	0.010	0.973	-	-
NDVI	-	-	-	-	0.959	−0.068	0.969	−0.023
LAI	-	-	-	-	0.941	−0.058	0.960	−0.047

Table 4. The contributions of factors for z_{0m} .

Site	Items	Component	Rotation Sums of Squared Loadings		
			Eigen Value	Variance Contribution (%)	Cumulative Variance Contribution (%)
Arou	Half-hourly z_{0m}	A_factor	1.971	44.03	44.03
		T_factor	1.202	38.33	82.36
Guantan	Half-hourly z_{0m}	A_factor	1.706	42.87	42.87
		T_factor	1.280	38.66	81.53

Table 4. Cont.

Site	Items	Component	Rotation Sums of Squared Loadings		
			Eigen Value	Variance Contribution (%)	Cumulative Variance Contribution (%)
Daman	Half-hourly z_{0m}	V_factor	2.125	53.14	53.14
		A_factor	1.052	30.29	83.43
	Daily z_{0m}	V_factor	2.178	54.46	54.46
		A_factor	1.057	30.67	85.13

4.3. Contributions of Driving Factors to Daily z_{0m}

The KMO value for daily z_{0m} at the Daman site is 0.731, which satisfies the minimal requirement (>0.5). The Bartlett’s sphericity test value is 333.777 and the p value is 0. Both the KMO test and Bartlett’s sphericity test demonstrate the feasibility of the data for factor analysis. Similar to the results of half-hourly z_{0m} , the first common factor for daily z_{0m} at the Daman site is the vegetation factor, which is composed of NDVI and LAI with factor loads of 0.969 and 0.960, respectively. The contribution of the vegetation factor is 54.46%. The contribution of the aerodynamic factor is 30.67%.

5. Discussion

5.1. The Applicability of Monin–Obukhov Similarity

In this research, we adopted a traditional method of calculating observed z_{0m} by fitting the profile observations using Monin–Obukhov similarity (MOS). As MOS was developed under homogeneous and flat underlying conditions, the applicability of MOS at the Arou and Guantanamo sites, which are located in mountainous areas, needs to be examined further. We filter the profiles with minimum wind velocity over 1 m/s and separate the wind speed data of one certain layer (20 m at the Arou site and 2 m at the Guantanamo site) as the target for validation. The remainder of the profiles are used to calculate the friction velocity, the displacement height and the aerodynamic roughness length in the MOS framework. Then, the wind speed of the target layer can be calculated accordingly. Figure 2 shows the linear fitting relationships between the measured wind speed and the calculated wind speed of the target layer: the coefficients of determination (R^2) values of the fitted equations are 0.95 and 0.68 for the Arou site and the Guantanamo site, respectively, indicating significant relationships between the measured wind speed and the calculated wind speed at both sites, confirming the applicability of MOS.

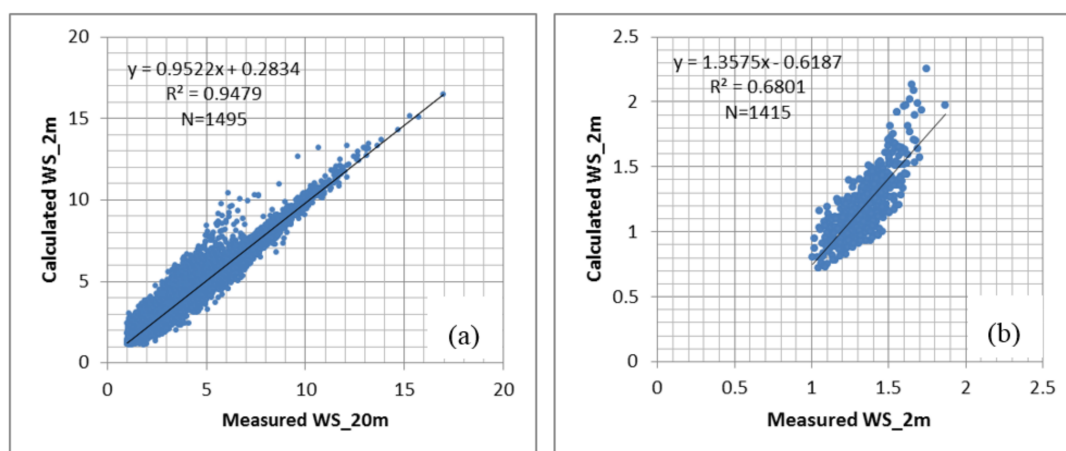


Figure 2. The distribution of scatters at (a) Arou site and (b) Guantanamo site between measured wind speed and calculated wind speed with Monin–Obukhov (MOS).

5.2. The Wind Speed Factor

To formulate the detailed change rule between z_{0m} and wind speed, we select the measured AWS data in August, when the vegetation reaches its peak-growth stage. The averaged z_{0m} values and standard deviations are calculated at 0.1 m/s wind speed intervals. Figure 3 reveals that the z_{0m} values decrease with increasing wind speed. The reduction in z_{0m} as the wind speed increases is most significant at the Arou site, and to a certain extent, the z_{0m} values remain relatively low and stable when the wind speeds become high (Figure 3a). Because of the barrier effects of the densely distributed stands of spruce around the Guantan site, the maximum wind speed in August is just over 4 m/s; thus, the descending z_{0m} trend is not pronounced (Figure 3b). At the Daman site, z_{0m} has a slowly descending tendency that is significantly correlated with increased wind speeds (Figure 3c). At slow wind speeds, the standard deviations of z_{0m} at all the stations are generally larger, possibly because the weak wind creates irregular turbulence inside the vegetation, resulting in large variations of z_{0m} under similar wind speed conditions.

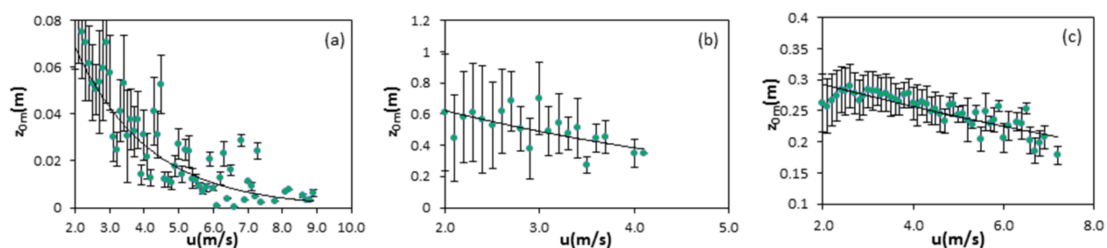


Figure 3. Distribution of half-hourly z_{0m} under variant wind speed scope at (a) Arou station; (b) Guantan station and (c) Daman station. Error bars centred at each data point indicate 95% confidence intervals of the regression estimate; an exponential trend line is added for each data series.

The most likely explanations for the decrease in aerodynamic roughness with increasing wind speed are as follows: as the wind speed increases, the wind changes the geometry of nonrigid bodies (such as vegetation) above the ground surface to some extent. In other words, as the stalks or blades of a plant lean in the same direction under wind action, the airflow drag due to the rough elements decreases; as the wind speed continues to increase, there is a critical point at which the plants reach equilibrium and their shapes no longer change with the wind speed. When the observed wind speed is small, the z_{0m} measured at the Guantan and Daman sites never reach this stable stage, whereas, at Arou, the z_{0m} measurements reflect this equilibrium.

5.3. The Wind Direction Factor

The influence of wind direction under unstable conditions was also explored to assess the homogeneity of these three sites. We plotted the distributions of half-hourly wind speed under different wind directions on polar coordinates; the frequency percentages of z_{0m} were classified at eight common wind directions (N-NE-E-SE-S-SW-W-NW). As Figure 4a shows, the dominant prevailing winds are west and southeast at the Arou site. Although the wind speed values are similar, significant differences occur in the z_{0m} between these two wind directions (Figure 4b): under a west wind, 98% of the z_{0m} values are less than 0.04 m, while under a southeast wind, 58% of the z_{0m} values under exceed 0.04 m. Therefore, easterly winds tend to result in larger z_{0m} values at the Arou site. At the Guantan site, wind is concentrated in two opposite directions, which can be partially explained by the mountains around the site. The z_{0m} values under the different wind directions also vary significantly (Figure 5b). Under south and southeast winds, approximately 80% of the z_{0m} values are less than 0.4 m. In contrast, under a northwest wind, 90% of the z_{0m} values are greater than 0.4 m. These results occur because the Guantan site is located on the shady slope of the mountain; thus, wind blowing directly against the slope results in larger z_{0m} values. The Daman site is located

in an irrigated flat farm area where the topography has little influence on the wind. The prevailing wind directions in August are southeast and northwest, and there is no significant difference in the frequency distribution of z_{0m} between the different wind directions, as shown in Figure 6b.

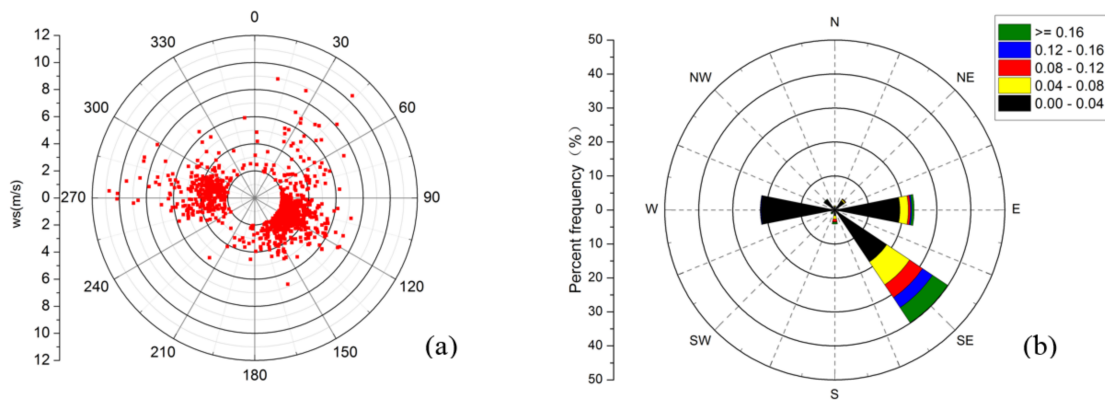


Figure 4. (a) Distribution map of half-hourly wind speed data and (b) half-hourly z_{0m} rose-binned data map at Arou station in August.

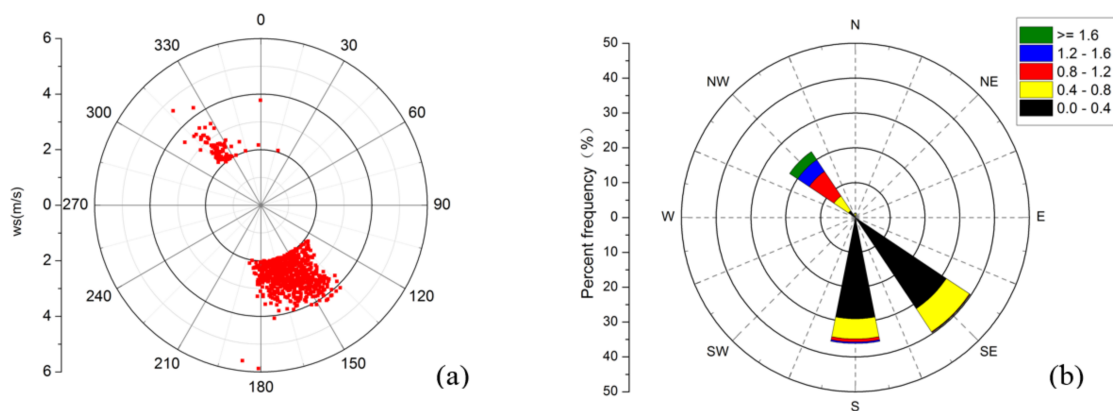


Figure 5. (a) Distribution map of half-hourly wind speed data and (b) half-hourly z_{0m} rose-binned data map at Guantan station in August.

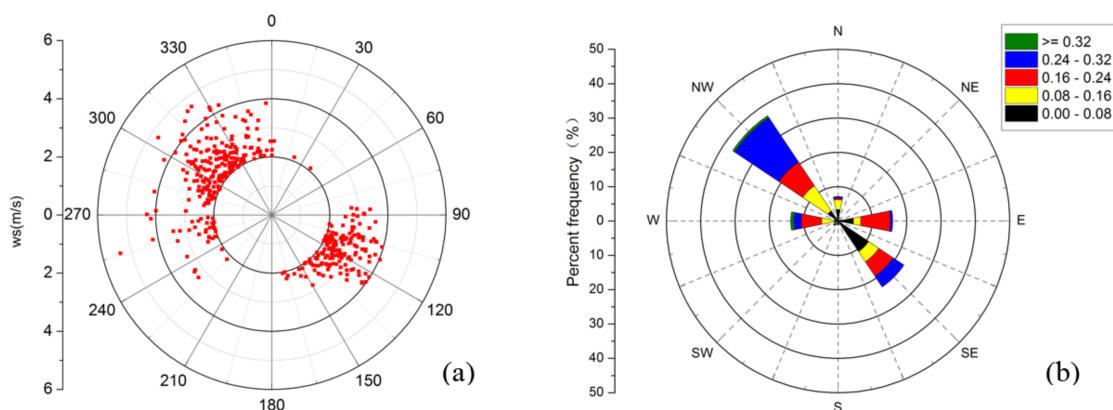


Figure 6. (a) Distribution map of half-hourly wind speed data and (b) half-hourly z_{0m} rose-binned data map at Daman station in August.

Table 5 shows the mean values of z_{0m} in August calculated at the two prevailing wind directions at each site and shows that the z_{0m} values at Arou and Guantan site differ significantly with wind

direction, while those at the Daman site are similar even under two opposite wind directions. Considering that the topographic relief of the entire source area is more prominent at Arou and Guantan sites compared with that at the Daman site, the z_{0m} influences from changes in wind direction may depend on the heterogeneity of the topography. For areas with complicated terrain, the density and distribution of rough elements presented to each wind direction differ; therefore, the drag forces near the earth's surface also differ, resulting in z_{0m} variations under different wind directions. However, in the area surrounding the Daman site, maize crops are planted in the homogeneous underlying surface; the densely distributed plants tend to flatten the small rough elements, leading to few z_{0m} effects from wind direction. In conclusion, wind direction is a main driving factor for z_{0m} in mountainous areas but can be ignored when modelling z_{0m} over flat surfaces underlying homogenous vegetation.

Table 5. Statistical table of averaged z_{0m} under prevailing wind direction.

$\overline{z_{0m}}$	Arou	Guantan	Daman
primary wind direction	0.072(SE)	0.349(SE)	0.237(NW)
secondary wind direction	0.009(W)	1.021(NW)	0.215(SE)

5.4. The Atmospheric Stability Factor

In previous studies, most researchers tend to filter z_{0m} under neutral conditions to simplify the z_{0m} estimation models, which are built on the assumption that z_{0m} under neutral conditions can represent the average level and that z_{0m} is not significantly different under different atmospheric conditions. However, based on the results of our factor analysis, this assumption might be incorrect. As listed in Table 6, the Obukhov lengths are binned by stability class to simplify analysis. Although the definition of the stability bins varies with local environmental conditions, these definitions have previously been used by authors [37,38]. The different atmospheric stability conditions in August are counted and presented by the frequency pie chart in Figure 7. The stable condition percentage is highest at the Arou and Daman sites, while unstable conditions form the highest proportion at the Guantan site. However, the neutral condition comprises only a small portion of all sites; therefore, the z_{0m} value under the neutral condition is not representative, especially for instantaneous flux calculations.

Table 6. Classification of atmospheric stability.

Atmospheric Condition	Definition
Stable	$0 < L < 1000$
Unstable	$-1000 < L < 0$
Neutral	$L < -1000$ or $L > 1000$

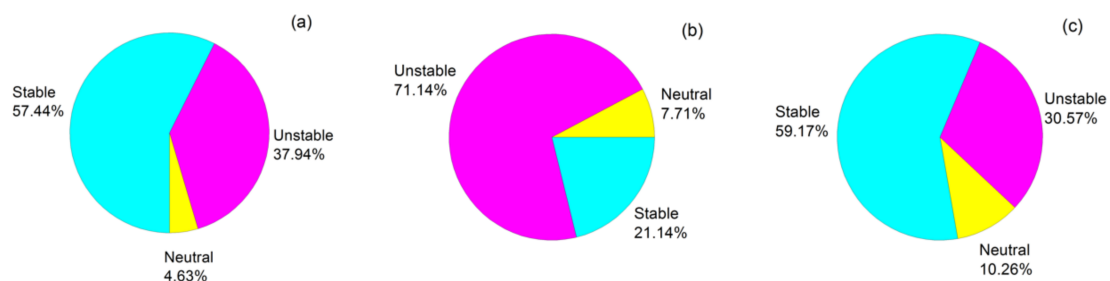


Figure 7. Frequency pie chart of different stabilities at the (a) Arou site; (b) Guantan site and (c) Daman site.

Figure 8 shows the distribution of half-hourly z_{0m} in August for stable, unstable and neutral conditions. Obviously, z_{0m} presents clear differences under different stability conditions at each site.

Because neutral conditions accounted for the smallest percentage, there are not enough samples to ensure that z_{0m} is normally distributed under these conditions. A comparison of these results shows that the averaged z_{0m} under stable conditions has the highest value, followed by that under neutral conditions, and the lowest values appear under unstable conditions. Under stable conditions, the z_{0m} values have a border value range and are distributed in a nearly normal fashion. Actually, atmospheric stability is closely related to the alternation of day and night. In the daytime, affected by the solar radiation, turbulent exchanges occur frequently between vegetation and the atmosphere and unstable atmospheric conditions are prominent; therefore, z_{0m} maintains low levels. At night, the atmospheric turbulence weakens, and z_{0m} increases significantly under the more stable conditions. In addition, because the relative frequencies of z_{0m} are similarly distributed among these three sites, we deduce that the influence on z_{0m} caused by atmospheric stability has nothing to do with the underlying surface.

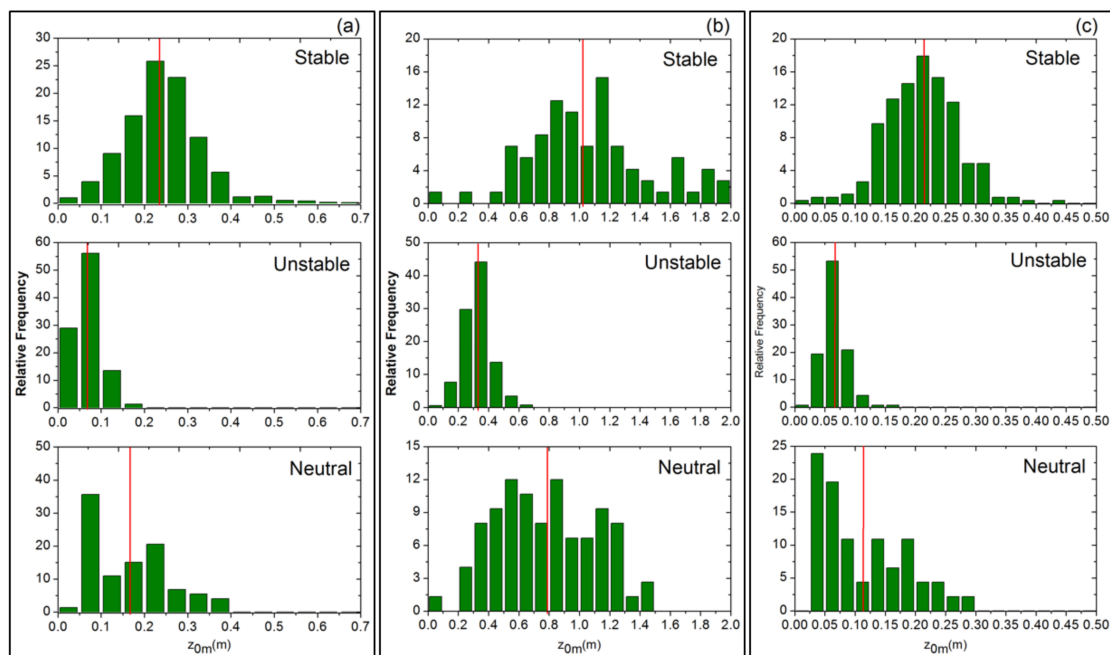


Figure 8. Relative frequency of z_{0m} for stable, unstable and neutral conditions at the (a) Arou site; (b) Guantan site and (c) Daman site. The vertical red lines in each image indicate the mean values.

6. Conclusions

This study statistically investigated the driving factors that influence z_{0m} at different time scales using three AWSs in the Heihe river basin that collect data for different land surface patterns. Aerodynamic factors, including wind speed and Obukhov length, are the main driving forces for the half-hourly changes in z_{0m} at the Arou Site and Guantan site, contributing 44.03% and 42.87%, respectively, at those sites, while topographic factors linked to the wind deflection angle contribute 38.33% and 38.66% to the half-hourly changes in z_{0m} at the two sites, respectively. Regarding the daily z_{0m} at the Arou and Guantan sites, only wind speed and wind deflection angle are correlating factors. The driving factors for half-hourly z_{0m} at the Daman site include both vegetation and aerodynamic factors, with contributions of 53.14% and 30.29%, respectively. Similar results were found for the daily z_{0m} at Daman site, except that atmospheric stability was not considered. It should be noted that vegetation factors such as NDVI and LAI have no significant relationship with either the half-hourly z_{0m} or the daily z_{0m} at the Arou and Guantan sites, but these vegetation factors are the primary driving factors for the Daman site, probably because of fewer changes in the botanical characteristics of grass and forest over growing seasons compared with the rapid changes due to crop growth in farmland.

Researchers should recognize that meteorological factors cannot be neglected in z_{0m} estimation models, especially for instantaneous flux simulations.

However, there are still some uncertainties in the results. First, this study focused only on the changes of z_{0m} during the vegetative growth period; consequently, which factors are most influential in other seasons is still unclear. Second, the factors tested in this paper are not comprehensive due to data source limitations; therefore, more factors that may influence z_{0m} should be taken into account. Third, the displacement height d , as the other important roughness parameter, is discussed relatively little in this paper; and the correlation between instantaneous d and z_{0m} may influence the accuracy of the observed z_{0m} . Thus, the driving factors of d and z_{0m} need to be examined at more sites with a wider variety of underlying surface and climate features to improve the robustness of the conclusions.

Acknowledgments: This work was supported by National Key R&D Program of China (No. 2016YFA0600304) and the Advanced Science Foundation Research Project of the Chinese Academy of Sciences (Grant No.: QYZDY-SSW-DQC014). The authors thank the Environmental and Ecological Science Data Center for West China, National Natural Science Foundation of China for providing the AWS data (<http://westdc.westgis.ac.cn>).

Author Contributions: Mingzhao Yu contributed to the research experiments, analysed the data, and wrote the paper. Bingfang Wu conceived the experiments, and was responsible for the research analysis. Hongwei Zeng, Qiang Xing and Weiwei Zhu collected and pre-processed the original data. All the co-authors helped to revise the manuscript.

Conflicts of Interest: The authors declare no conflict of interest.

References

1. Stull, R.B. An Introduction to Boundary Layer Meteorology. *Atmos. Sci. Libr.* **1988**, *8*, 89.
2. Hryama, T.; Sugita, M.; Kotoda, K. Regional Roughness Parameters and Momentum Fluxes over a Complex Area. *J. Appl. Meteorol.* **1996**, *35*, 336–347. [[CrossRef](#)]
3. Marticorena, B.; Kardous, M.; Bergametti, G.; Callot, Y.; Chazette, P.; Khatteli, H.; Le Hégarat-Masclé, S.; Maillé, M.; Rajot, J.; Vidal-Madjar, D.; et al. Surface and aerodynamic roughness in arid and semiarid areas and their relation to radar backscatter coefficient. *J. Geophys. Res. Earth Surf.* **2006**, *111*. [[CrossRef](#)]
4. Monteith, J.L. The micrometeorology of crops. In *Principles of Environmental Physics*; Edward Arnold: London, UK, 1973; pp. 190–215.
5. Brutsaert, W. *Evaporation into the Atmosphere; Theory, History, and Applications*; Springer: Dordrecht, The Netherlands, 1982.
6. Raupach, M.R. Drag and drag partition on rough surfaces. *Bound. Layer Meteorol.* **1992**, *60*, 375–395. [[CrossRef](#)]
7. Raupach, M. Simplified expressions for vegetation roughness length and zero-plane displacement as functions of canopy height and area index. *Bound. Layer Meteorol.* **1994**, *71*, 211–216. [[CrossRef](#)]
8. Schmid, H.P.; Bünzli, B. The influence of surface texture on the effective roughness length. *Q. J. R. Meteorol. Soc.* **1995**, *121*, 1–21. [[CrossRef](#)]
9. Gupta, R.K.; Prasad, T.S.; Vijayan, D. Estimation of roughness length and sensible heat flux from WiFS and NOAA AVHRR data. *Adv. Sp. Res.* **2002**, *29*, 33–38. [[CrossRef](#)]
10. Choudhury, B.J.; Monteith, J.L. A four-layer model for the heat budget of homogeneous land surfaces. *Q. J. R. Meteorol. Soc.* **1988**, *114*, 373–398. [[CrossRef](#)]
11. Yu, M.; Wu, B.; Yan, N.; Xing, Q.; Zhu, W. A Method for Estimating the Aerodynamic Roughness Length with NDVI and BRDF Signatures Using Multi-Temporal Proba-V Data. *Remote Sens.* **2016**, *9*, 6. [[CrossRef](#)]
12. Colin, J.; Menenti, M.; Rubio, E.; Jochum, A. Accuracy vs. Operability: A Case Study over Barrax in the Context of the DEMETER Project. *AIP Conf. Proc.* **2006**, *852*, 75–83.
13. Jasinski, M.F.; Borak, J.; Crago, R. Bulk surface momentum parameters for satellite-derived vegetation fields. *Agric. For. Meteorol.* **2005**, *133*, 55–68. [[CrossRef](#)]
14. Zhou, Y.L.; Sun, X.M.; Zhang, R.H.; Zhu, Z.L.; Xu, J.P.; Li, Z.L. The improvement and validation of the model for retrieving the effective roughness length on TM pixel scale. In *Proceedings of the IEEE International Geoscience and Remote Sensing Symposium*, Seoul, Korea, 25–29 July 2005; pp. 3059–3062.
15. Zhou, Y.L. Surface Roughness Length Dynamic and Its Effects on Fluxes Simulation. Ph.D. Thesis, Institute of Geographic Sciences and Natural Resources Research, CAS, Beijing, China, 2008.

16. Gao, Y.; Hu, Y. *Advances in HEIFE Research (1987–1994)*; China Meteorological Press: Beijing, China, 1994.
17. Li, X.; Li, X.W.; Li, Z.; Ma, M.; Wang, J.; Xiao, Q.; Liu, Q.; Che, T.; Chen, E.; Yan, G.; et al. Watershed allied telemetry experimental research. *J. Geophys. Res. Atmos.* **2009**, *114*, 2191–2196. [[CrossRef](#)]
18. Liu, X.; Cheng, G.D.; Liu, S.M.; Xiao, Q.; Ma, M.; Jin, R.; Che, T.; Liu, Q.; Wang, W.; Qi, Y.; et al. Heihe watershed allied telemetry experimental research (Hiwater): Scientific objectives and experimental design. *Bull. Am. Meteorol. Soc.* **2013**, *94*, 1145–1160. [[CrossRef](#)]
19. Mingguo, M.; Weizhen, W.; Junlei, T.; Guanghui, H.; Zhihui, Z. *WATER: Dataset of Automatic Meteorological Observations at the Dayekou Guantan Forest Station in the Dayekou Watershed*; Cold and Arid Regions Environmental and Engineering Research Institute, Chinese Academy of Sciences: Beijing, China, 2008.
20. Liu, S.M.; Xu, Z.W.; Wang, W.Z.; Jia, Z.Z.; Zhu, M.J.; Bai, J.; Wang, J.M. A comparison of eddy-covariance and large aperture scintillometer measurements with respect to the energy balance closure problem. *Hydrol. Earth Syst. Sci.* **2011**, *15*, 1291–1306. [[CrossRef](#)]
21. Chen, J.; Jönsson, P.; Tamura, M.; Gu, Z.; Matsushita, B.; Eklundh, L. A simple method for reconstructing a high-quality NDVI time-series data set based on the Savitzky-Golay filter. *Remote Sens. Environ.* **2004**, *91*, 332–344. [[CrossRef](#)]
22. Yin, G.; Li, J.; Liu, Q.; Fan, W.; Xu, B.; Zeng, Y.; Zhao, J. Regional Leaf Area Index Retrieval Based on Remote Sensing: The Role of Radiative Transfer Model Selection. *Remote Sens.* **2015**, *7*, 4604–4625. [[CrossRef](#)]
23. Yin, G.; Li, J.; Liu, Q.; Zhong, B.; Li, A. Improving LAI spatio-temporal continuity using a combination of MODIS and MERSI data. *Remote Sens. Lett.* **2016**, *7*, 771–780. [[CrossRef](#)]
24. Li, X.; Liu, S.M.; Xiao, Q.; Ma, M.G.; Jin, R.; Che, T.; Wang, W.Z.; Hu, X.L.; Xu, Z.W.; Wen, J.G.; et al. A multiscale dataset for understanding complex eco-hydrological processes in a heterogeneous oasis system. *Sci. Data* **2017**, *4*, 170083. [[CrossRef](#)] [[PubMed](#)]
25. Argyle, P.; Watson, S.J. Assessing the dependence of surface layer atmospheric stability on measurement height at offshore locations. *J. Wind Eng. Ind. Aerodyn.* **2014**, *131*, 88–99. [[CrossRef](#)]
26. Richardson, L.F. Some Measurements of Atmospheric Turbulence. *R. Soc.* **1921**, *221*, 582–593. [[CrossRef](#)]
27. Zhu, W.; Wu, B.; Yan, N.; Feng, X.; Xing, Q. A method to estimate diurnal surface soil heat flux from MODIS data for a sparse vegetation and bare soil. *J. Hydrol.* **2014**, *511*, 139–150. [[CrossRef](#)]
28. Panofsky, H.A. Determination of stress from wind and temperature measurement. *Q. J. R. Meteorol. Soc.* **1963**, *89*, 85–94. [[CrossRef](#)]
29. Dyer, A.J. A review of flux-profile relationships. *Bound. Layer Meteorol.* **1974**, *7*, 363–372. [[CrossRef](#)]
30. Webb, E.K. Profile relationships: The log-linear range, and extension to strong stability. *Q. J. R. Meteorol. Soc.* **1970**, *96*, 67–90. [[CrossRef](#)]
31. Frangi, J.P.; Richard, D.C. The WELSONS experiment: Overview and presentation of first results on the surface atmospheric boundary-layer in semiarid Spain. *Ann. Geophys.* **2000**, *18*, 365–384. [[CrossRef](#)]
32. Zhou, Y.; Ju, W.; Sun, X.; Wen, X.; Guan, D. Significant decrease of uncertainties in sensible heat flux simulation using temporally variable aerodynamic roughness in two typical forest ecosystems of China. *J. Appl. Meteorol. Climatol.* **2012**, *51*, 1099–1110. [[CrossRef](#)]
33. Pielke, S.; Roger, A. *Mesoscale Meteorological Modeling*; Academic Press: Cambridge, MA, USA, 2013; Volume 98.
34. Zou, M.; Niu, J.; Kang, S.; Li, X.; Lu, S. The contribution of human agricultural activities to increasing evapotranspiration is significantly greater than climate change effect over Heihe agricultural region. *Sci. Rep.* **2017**, *7*, 8805. [[CrossRef](#)] [[PubMed](#)]
35. Kaiser, H.F. An index of factorial simplicity. *Psychometrika* **1974**, *39*, 31–36. [[CrossRef](#)]
36. Bartlett, M.S. Properties of Sufficiency and Statistical Tests. *Proc. R. Soc. Lond.* **1937**, *160*, 268–282. [[CrossRef](#)]
37. Motta, M.; Barthelmie, R.J.; Vølund, P. The influence of non-logarithmic wind speed profiles on potential power output at Danish offshore sites. *Wind Energy* **2005**, *8*, 219–236. [[CrossRef](#)]
38. Muñozesparza, D.; Cañadillas, B.; Neumann, T.; van Beeck, J. Turbulent fluxes, stability and shear in the offshore environment: Mesoscale modelling and field observations at FINO1. *J. Renew. Sustain. Energy* **2012**, *4*, 063136. [[CrossRef](#)]

